Moisture transfer by turbulent natural convection

Lu Zhang[1,2], Kai Leong Chong[1] and Ke-Qing Xia[2,1],†

[1]Department of Physics, The Chinese University of Hong Kong, Shatin, Hong Kong, China

[2]Center for Complex Flows and Soft Matter Research and Department of Mechanics and Aerospace Engineering, Southern University of Science and Technology, Shenzhen, 518055, China

We present an experimental and numerical study of natural convection with moist air as convecting fluid. By simplifying the system as two-component convection, an experimental method is proposed for indirectly measuring the moisture transfer rates in buoyancy-driven flows. We verify the results using direct numerical simulations. It is found that the non-dimensionalized transfer rates for both sensible heat (Nu_T) and water vapour (Nu_e) are essentially determined by a generalized Grashof number Gr (the ratio of combined buoyancy generated by the imposed temperature and vapour pressure gradients to viscous force), and are only weakly dependent on the buoyancy ratio Λ (the ratio of buoyancy induced by temperature variation to that due to vapour pressure variation). Moreover, we show that the full set of control parameters $\{Gr, \Lambda, Pr, Sc\}$ is more suitable than other choices for characterizing the two-component system under investigation. As a special case, the Schmidt number dependence for passive scalar transport rates in buoyancy-driven flows is also deduced.

Key words: condensation/evaporation, moist convection

1. Introduction

Mass, heat and momentum transfers in turbulent flows occur widely in nature, and very often they are coupled to each other. Examples include thermohaline convection in ocean circulation (Huppert & Turner 1981; Gent & Mcwilliams 1990; Schmitt 1994), pollutant dispersion in the atmosphere (Sini, Anquetin & Mestayer 1996; Arya 1999) and heat and moisture transfers in ocean evaporation (Liu 1979; Fairall *et al.* 1996, 2003). The last example has vital significances for both the global water cycle and climate change (Cane *et al.* 1997; Levitus *et al.* 2000; Durack, Wijffels & Matear 2012), since evaporation is the major source of atmospheric water (Maidment 1993). In such a case, the transports of heat and mass are strongly coupled to each other, which makes the problem more difficult. Owing to the intrinsic complexity, measurements of transport properties of heat and mass in turbulent flows are, to our knowledge, scarce. In this paper we take evaporation above a fluid layer driven by natural convection (in the form of the classical Rayleigh–Bénard (RB) configuration) as an example and present an experimental method for indirectly measuring the

† Email address for correspondence: xiakq@sustech.edu.cn

mass transfer rates of water vapour. We then verify the measured results with direct numerical simulations (DNS). Owing to its well-defined boundary conditions and precisely tunable control parameters, RB convection has become a paradigmatic system in the studies of various convection phenomena occurring in nature (Ahlers, Grossmann & Lohse 2009; Lohse & Xia 2010; Chillà & Schumacher 2012; Xia 2013).

Classical turbulent RB convection concerns a fluid layer cooled from above and heated at the bottom. However, in atmospheric convection, the situation is more complicated (Emanuel 1994). The key difference between atmospheric convection and RB convection is that the water in the atmosphere undergoes phase transition. Water evaporates from the Earth's surface and will rise and condense at a certain height. Condensation of water vapour is accompanied by the release of latent heat, which results in a lower adiabatic lapse rate. Moreover, clouds formed by suspensions of the condensed water droplets will also affect the albedo and energy budget (Bodenschatz *et al.* 2010; Chandrakar *et al.* 2016). Developments of moist RB convection have been made to shed light on atmospheric convection. For example, Bretherton (1987, 1988) developed an idealized model of non-precipitating moist convection. Schumacher & Pauluis (2010), Weidauer, Pauluis & Schumacher (2010) and Pauluis & Schumacher (2011) used a piecewise linear buoyancy equation to study moist convection in a conditionally unstable regime. Hernandez-Duenas *et al.* (2013), on the other hand, proposed a minimal model that allows rain water to fall. More recently, Vallis, Parker & Tobias (2019) presented an idealized model of moist convection by adding a condensation term which obeys a simplified Clausius–Clapeyron relation.

In this paper, we focus on the mass transfer properties of water in a moist turbulent convection system. The remainder of the paper is organized as follows. We first describe our experimental method in § 2. In § 3 we introduce the governing equations. The correction for sidewall condensation is then described in § 4. We then verify our experimental results using DNS in § 5. The effect of density ratio is discussed in § 6. Based on the results in § 6, we deduce in § 7 the Schmidt number dependence of the transport efficiency when one of the scalars is passive. Our results are compared with a generalized Grossmann–Lohse theory in § 8. We then show the implications for evaporation in nature in § 9 and finally conclude our work in § 10.

2. Method

In the experiment, a rectangular RB convection cell with dimensions 12.6 cm (height) × 12.6 cm (length) × 7.6 cm (width) is used. The system consists of a thin layer (1.6 cm in thickness) of distilled and deionized water at the bottom, with moist air above filling the rest of the cell. The system is kept at atmospheric pressure and the mixture of water vapour and dry air can be treated as an ideal gas. The top and bottom plates are made of copper. The top plate is cooled by a temperature-regulated refrigerator and the bottom plate is heated by a resistive heater. Three thermistors (0.7 cm away from the liquid–solid interface) are embedded in the plates to monitor the temperature therein, denoted by $T_{p,bot}$ and $T_{p,top}$. An additional small thermistor (see figure 1) is placed in the centre of the liquid water layer in order to monitor the temperature in the centre of the liquid layer $T_{l,c}$. When the bottom plate is heated and the top plate is cooled, a temperature gradient will be built in the thin water layer. The temperature at the liquid–gas interface is then determined by $T_{bot} = 2T_{l,c} - T_{p,bot}$. Water evaporates at the bottom liquid–gas interface and condenses on the top plate, forming a thin layer of liquid water thereon (Zhong, Funfschilling & Ahlers 2009;
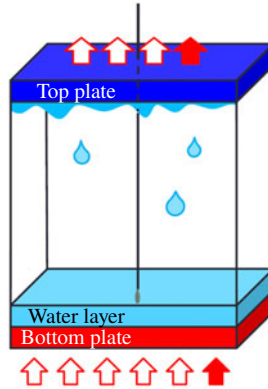
FIGURE 1. (Colour online) Schematic of the experimental set-up. Arrows indicate the direction of heat flux. Open arrows denote the LHF and the filled arrows represent the SHF.

Prabhakaran *et al.* 2017). In steady state, the upward mass flux of water vapour is balanced by the downward-dripping droplets. Since the top liquid–gas interface is a dynamic one and therefore difficult to measure directly, we approximate its temperature by $T_{top} = T_{p,top}$. During the experiment, the whole convection cell is placed in a home-made thermostat whose temperature is set to be the same as the bulk temperature of the mixture. The temperature stability of the thermostat is about ± 0.02 K. Data acquisition is made after all temperature signals reach statistical stationary states, and each heat transfer measurement lasts for more than two hours.

The total heat flux in this system can be divided into two parts, the sensible heat flux (SHF) and the latent heat flux (LHF) (Mangarella *et al.* 1973) (see figure 1). The former is what is typically measured in RB convection experiments (Ahlers *et al.* 2009; Lohse & Xia 2010) and the latter reflects the contribution of phase transition at both boundaries. It is with this LHF that we deduce the mass flux, or vapour transfer rate.

Since the system is free of condensation nuclei and far from the critical point, we expect that neither heterogeneous (Chandrakar *et al.* 2016) nor homogeneous condensations (Prabhakaran *et al.* 2017) would occur in the bulk region of the convection cell. This fact was verified by a laser light scattering test, in which no visible droplets were observed. The total heat flux Φ_q can then be approximated as

$$\Phi_q = \Phi_S + \Phi_L = (Nu_T k \Delta_T + Nu_e DL \Delta_{\rho,v})/H. \tag{2.1}$$

Here, $Nu_T = \Phi_S H/(k\Delta_T)$ and $Nu_e = \Phi_L H/(DL\Delta_{\rho,v})$ are the Nusselt numbers for temperature and vapour pressure, respectively. They represent the non-dimensionalized heat and moisture transfer rates. In the above, Φ_S is the SHF and Φ_L is the LHF. Parameters k and D are the thermal conductivity and mass diffusivity of water vapour in dry air and L is the latent heat of water. The difference $\Delta_T = T_{bot} - T_{top}$ is the temperature difference across the layer of moist air, with T_{bot} the temperature at the lower liquid–gas interface and T_{top} the temperature at the upper liquid–gas interface. In the above, $\Delta_{\rho,v}$ denotes the water vapour density difference across the two liquid–gas interfaces, which can be further written as $\Delta_{\rho,v} = (e_{s,bot}/T_{bot} - e_{s,top}/T_{top})M_e/R$. Here $e_{s,bot}$ and $e_{s,top}$ are the saturation water vapour pressures at the bottom and top
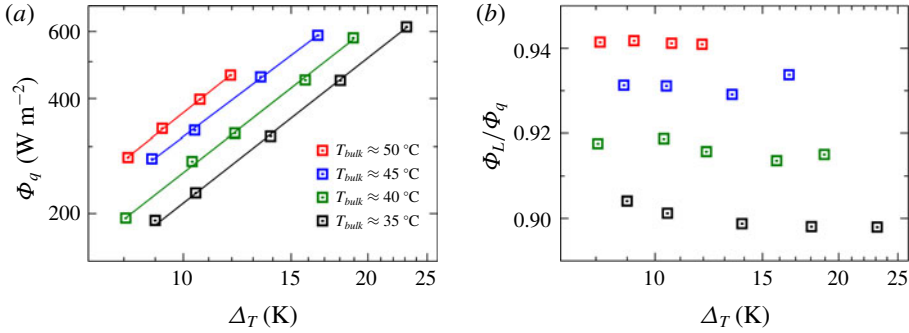
FIGURE 2. (Colour online) (*a*) Total heat flux Φ_q as a function of the temperature difference Δ_T across the two liquid–gas interfaces, and for various values of the bulk temperature T_{bulk} which is measured at the cell centre. (*b*) The ratio of the LHF to the total heat flux Φ_L/Φ_q.

interfaces, with M_e the molar mass of water vapour and R the universal gas constant. We plot in figure 2(*a*) the experimentally measured total heat flux Φ_q as a function of the temperature difference across the two liquid–gas interfaces. It is seen that Φ_q shows an excellent power-law dependence on Δ_T. Meanwhile, for a fixed Δ_T, higher bulk temperature leads to a higher total heat flux. This can be understood by the fact that the difference of the saturation water vapour pressure between the two boundaries $(\Delta_{\rho,v})$ increases as bulk temperature is raised (Murray 1967), so the corresponding LHF also increases. It is worth mentioning that since the latent heat of water is large, LHF accounts for over 90 % of the total heat flux in the parameter range explored in our experiment, as illustrated in figure 2(*b*). So LHF is the dominant factor in (2.1) for the present case.

3. Governing equations

To obtain the moisture transfer rate Nu_e, we first consider the governing equations of the system. These equations can be derived (Landau & Lifshitz 2013) by choosing temperature T and water vapour pressure e as state variables and applying the Oberbeck–Boussinesq approximation, $\rho(T, e) = \rho_0[1 - \alpha(T - T_0) - \beta(e - e_0)] = \rho_0(1 - \alpha\delta T - \beta\delta e)$, where T_0 and e_0 are the reference temperature and vapour pressure, which are usually taken to be their respective bulk values; $\alpha \equiv -\partial\rho/\partial T$ and $\beta \equiv -\partial\rho/\partial e$ are the thermal expansion coefficient and the solutal expansion coefficient, respectively. These coefficients can be determined from the equation of state of the moist mixture: $\rho = [eM_e + (P_0 - e)M_d]/(RT)$ (Andrews 2000). Here M_d is the molar mass of dry air and P_0 is the atmospheric pressure. With this approximation, the buoyancy term in the usual Oberbeck–Boussinesq equations for classical RB convection becomes $(\alpha\delta T + \beta\delta e)\boldsymbol{g}$. In addition, there is now also a diffusion–convection equation for e which is the same as that for T except κ is replaced by D. Putting together, one has the following governing equations:

$$\frac{\partial \boldsymbol{u}}{\partial t} + \boldsymbol{u} \cdot \boldsymbol{\nabla}\boldsymbol{u} = -\frac{1}{\rho}\boldsymbol{\nabla}p + \nu\nabla^2\boldsymbol{u} + (\alpha\delta T + \beta\delta e)g\hat{\boldsymbol{k}}, \quad (3.1)$$

$$\frac{\partial T}{\partial t} + \boldsymbol{u} \cdot \boldsymbol{\nabla}T = \kappa\nabla^2 T, \quad (3.2)$$

$$\frac{\partial e}{\partial t} + \boldsymbol{u} \cdot \nabla e = D \nabla^2 e, \tag{3.3}$$

$$\nabla \cdot \boldsymbol{u} = 0. \tag{3.4}$$

To non-dimensionalize these equations, one can follow the idea developed in double-diffusive convection and, more recently, two-scalar convection system (Radko 2013; Yang, Verzicco & Lohse 2018), and get four control parameters, i.e. two Rayleigh numbers $Ra_T = \alpha g \Delta_T H^3/(\nu\kappa)$ and $Ra_e = \beta g \Delta_e H^3/(\nu D)$, Prandtl number $Pr = \nu/\kappa$ and Schmidt number $Sc = \nu/D$. Here Ra_T and Ra_e are Rayleigh numbers for the temperature and vapour pressure. They describe the relative driven strength induced by temperature difference and by vapour pressure drop, respectively.

Here, to better characterize this two-component convection system, we introduce a new type of non-dimensionlization for the governing equations by defining a generalized free-fall time $t = \sqrt{H/(\alpha\Delta_T g + \beta\Delta_e g)}$ as a typical time scale, and use cell height H, temperature difference Δ_T and vapour pressure difference $\Delta_e = e_{s,bot} - e_{s,top}$ as the other characteristic scales for the non-dimensionlization of related quantities. The non-dimensional governing equations read as

$$\frac{\partial \boldsymbol{u}'}{\partial t'} + \boldsymbol{u}' \cdot \nabla \boldsymbol{u}' = -\nabla p' + \sqrt{\frac{1}{Gr}} \nabla^2 \boldsymbol{u}' + \left(\frac{\Lambda}{\Lambda+1} T' + \frac{1}{\Lambda+1} e' \right) \hat{k}, \tag{3.5}$$

$$\frac{\partial T'}{\partial t'} + \boldsymbol{u}' \cdot \nabla T' = \sqrt{\frac{1}{Gr}} Pr^{-1} \nabla^2 T', \tag{3.6}$$

$$\frac{\partial e'}{\partial t'} + \boldsymbol{u}' \cdot \nabla e' = \sqrt{\frac{1}{Gr}} Sc^{-1} \nabla^2 e', \tag{3.7}$$

$$\nabla \cdot \boldsymbol{u}' = 0, \tag{3.8}$$

where $Gr = (\alpha\Delta_T + \beta\Delta_e)gH^3/\nu^2$ is a generalized Grashof number (Sanders & Holman 1972; Bergman *et al.* 2011), which represents the relative strength of the total buoyancy; $\Lambda = \alpha\Delta_T/(\beta\Delta_e)$ is the buoyancy ratio, or the ratio of buoyancy induced by temperature changes to that induced by changes in water vapour pressure; and Pr and Sc are the Prandtl number and Schmidt number, as usual. We note that, with the above normalization, the two scalars (T and e) are on equal footing, or symmetric, in the equations of motion. Parameters $\{Gr, \Lambda, Pr, Sc\}$ together with the aspect ratio Γ of the convection cell now form the full set of control parameters. The Grashof number and the buoyancy ratio can also be expressed in terms of the above Rayleigh numbers as $Gr = (Ra_T/Pr + Ra_e/Sc)$ and $\Lambda = (Ra_T/Pr)/(Ra_e/Sc)$, respectively.

For the moist mixture in the experiment, $Pr \simeq 0.7$ and $Sc \simeq 0.6$. Thus, the ratio between thermal diffusivity and mass diffusivity, namely the Lewis number $Le \equiv \kappa/D = Sc/Pr$, is about 1. Therefore, we may expect that the water vapour field is similar to the temperature field, which led us to make the approximation $Nu_e \simeq Nu_T$. Physically this means that, with equal diffusivity, heat and moisture are carried by the turbulent flow with the same efficiency, which is also evident from the equations of motion. Under this approximation, we can obtain Nu_e from the experimentally measured total heat flux. The results are shown as square symbols in figure 3. A correction has been made to account for the additional LHF leakage from the sidewall, as described below.
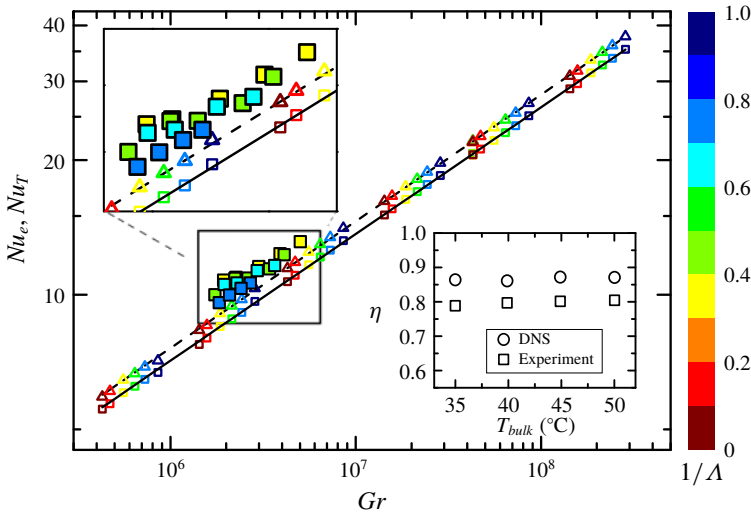
FIGURE 3. (Colour online) Nusselt numbers Nu_e and Nu_T as functions of the Grashof number Gr. Filled squares: experimentally measured Nu_e; open squares: Nu_e from DNS; solid line: $0.143Gr^{0.283}$, which is a power-law fit to Nu_e from DNS; open triangles: Nu_T from DNS; dashed line: $0.152Gr^{0.283}$, which is a power-law fit to Nu_T from DNS. The colour bar shows the inverse buoyancy ratio. The upper inset shows a magnified view containing the experimental data. Lower inset: squares, correction coefficient (4.2) used for correcting the experimental data; circles, correction coefficient obtained from DNS.

4. Correction for sidewall condensation

In an ideal case, water evaporates at the lower interface, being transported to the opposite side by turbulent convection and condenses therein. The sidewall is assumed to be adiabatic and free of condensation. Despite the thermal insulations used to prevent sensible heat leakage, condensation on the sidewall is inevitable and a correction for the latent heat leakage from the sidewall must be made, which was done as follows. The saturation water vapour pressure depends only on temperature and is determined by the Tetens empirical formula (Murray 1967): $e_s(T) = 6.1078 \times \exp[17.2693882(T - 273.16)/(T - 35.86)]$. The bulk temperature is simply the arithmetic mean of those at the interfaces: $T_{bulk} = (T_{bot} + T_{top})/2$. The bulk vapour pressure is approximated as

$$e_{bulk} = [(e_{s,bot} + e_{s,top}) \times S_{plate} + e_{s,sidewall} \times S_{sidewall}]/(2S_{plate} + S_{sidewall}), \qquad (4.1)$$

where S_{plate} and $S_{sidewall}$ are the areas of the conducting plate and the sidewall. For large aspect ratios, the above equation reduces to $e_{bulk} = (e_{s,bot} + e_{s,top})/2$. Since the saturation vapour pressure has an exponential dependence on temperature, the bulk vapour pressure is therefore higher than the corresponding saturation vapour pressure at bulk temperature $e_{bulk} > e_{s,T_{bulk}}$, which means there exists a vapour concentration boundary layer at the sidewall. By further assuming that the thickness of this boundary layer is the same as those over the two interfaces, the ratio of the LHF across the top liquid–gas interface to the total supply at the bottom plate can then be approximated as

$$\eta = \frac{\Phi_{eff}}{\Phi_{total}} = \frac{(e_{bulk} - e_{s,T_{top}}) \times S_{plate}}{(e_{bulk} - e_{s,T_{top}}) \times S_{plate} + (e_{bulk} - e_{s,T_{bulk}}) \times S_{sidewall}}. \qquad (4.2)$$

We used the average value of this ratio as a correction coefficient for the sidewall latent heat leakage, and obtained the corrected Nusselt number for water vapour as

$$Nu_e = \frac{\Phi_q}{k\Delta_T/H + \eta^{-1}DL\Delta_{\rho,v}/H}. \tag{4.3}$$

5. Verification by DNS

To verify this simplified two-component convection model, we use the CUPS code (Chong, Ding & Xia 2018) to solve (3.5)–(3.8) by a fourth-order finite-volume method on staggered grids. In addition, the simulations cover a much wider range of both Grashof number Gr and buoyancy ratio Λ than our experiment. The Prandtl number and the Schmidt number are fixed at $Pr = 0.7$ and $Sc = 0.6$. The DNS are conducted in a cubic domain. All boundaries are set to be impermeable and non-slip. Moreover, we apply constant-value boundary conditions at the top and bottom plates and zero-flux conditions at the sidewalls for both the temperature and the vapour fields. We also adopt a non-uniform mesh with denser grids at the boundaries (the grid spacing following a tanh function therein) in our simulations and use up to 256^3 grids for the highest Grashof number of 3×10^8, to ensure that both the Kolmogorov and Batchelor scales are resolved (Shishkina *et al.* 2010). The parameters as well as the time-averaged Nusselt number for both temperature and vapour can be found in table 1.

The DNS results for the moisture transfer Nusselt number Nu_e are shown as open squares in figure 3. It is seen that, under the present resolution, all data points with different buoyancy ratios fall on a singe solid line, $Nu_e = 0.143Gr^{0.283}$, which implies that the moisture transfer Nussult number Nu_e is mainly determined by the Grashof number Gr and is hardly affected by the buoyancy ratio Λ. In the same figure, we plot the sensible heat transfer Nussult number Nu_T as open triangles. It is seen that Nu_T exhibits the same scaling dependence on Gr as Nu_e, but with a slightly larger magnitude; a power-law fitting gives $Nu_T = 0.152Gr^{0.283}$. The difference between Nu_e and Nu_T is about 6 %. The fact that both Nu_e and Nu_T exhibit negligible dependence on the buoyancy ratio shows that the Grashof number is the primary control parameter in determining the transport properties of both scalars.

In the upper left-hand corner of figure 3, we show a magnified portion of the plot containing the experimental data (squares). It is seen that the experimentally determined moisture transfer rate Nu_e is in general higher than the corresponding DNS data. This difference may be attributed to the fact that, in our simulation, the upper boundary is treated as flat and non-slip. Whereas in the experiment, water condensed in the upper boundary forms a 'rough' liquid–gas interface and then drips down occasionally. Such effect is neglected for the moment and may introduce additional uncertainty. Wei *et al.* (2014) studied the heat transport in RB convection with smooth bottom and rough top plate, which is close to the situation in our present experiment. They found that the heat transport efficiency in such a configuration is slightly higher than that in the smooth–smooth cell and much lower than that in the rough–rough cell. On the other hand, the dripping event will undoubtedly induce a perturbation in the flow field and thus might trigger a burst of the heat flux. We can make an estimation as follows. Taking the point of the top right-hand corner in figure 2 as an example and considering that the SHF cannot exceed the total heat flux, the mass flux of water vapour is about $dm/dt = \Phi_L \times S/L < \Phi_q \times S/L \sim 6g/h$. Therefore, we consider that the effects of dripping are relatively small compared to the sidewall condensation as we discussed in § 4.

Pr	Sc	Ra_T	Ra_e	Λ	Gr	N_{grids}	Nu_T	Nu_e	t_{avg}
0.7	0.6	3×10^5	0	0	4.29×10^5	72^3	5.92	5.55	1000
0.7	0.6	3×10^5	2.57×10^4	0.1	4.71×10^5	72^3	6.09	5.71	1000
0.7	0.6	3×10^5	7.71×10^4	0.3	5.57×10^5	72^3	6.45	6.04	1000
0.7	0.6	3×10^5	1.29×10^5	0.5	6.43×10^5	72^3	6.67	6.24	1000
0.7	0.6	3×10^5	1.80×10^5	0.7	7.29×10^5	72^3	6.90	6.47	1000
0.7	0.6	3×10^5	2.57×10^5	1	8.57×10^5	72^3	7.12	6.70	1000
0.7	0.6	10^6	0	0	1.43×10^6	96^3	8.34	7.74	1000
0.7	0.6	10^6	8.57×10^4	0.1	1.57×10^6	96^3	8.55	8.00	1000
0.7	0.6	10^6	2.57×10^5	0.3	1.86×10^6	96^3	9.08	8.49	1000
0.7	0.6	10^6	4.29×10^5	0.5	2.14×10^6	96^3	9.44	8.84	1000
0.7	0.6	10^6	6×10^5	0.7	2.43×10^6	96^3	9.76	9.13	1000
0.7	0.6	10^6	8.57×10^5	1	2.86×10^6	96^3	10.3	9.67	1000
0.7	0.6	3×10^6	0	0	4.29×10^6	128^3	11.4	10.7	1000
0.7	0.6	3×10^6	2.57×10^5	0.1	4.71×10^6	128^3	11.8	11.1	1000
0.7	0.6	3×10^6	7.71×10^5	0.3	5.57×10^6	128^3	12.5	11.7	1000
0.7	0.6	3×10^6	1.29×10^6	0.5	6.43×10^6	128^3	13.0	12.1	1000
0.7	0.6	3×10^6	1.80×10^6	0.7	7.29×10^6	128^3	13.4	12.6	1000
0.7	0.6	3×10^6	2.57×10^6	1	8.57×10^6	128^3	14.1	13.2	1000
0.7	0.6	10^7	0	0	1.43×10^7	162^3	16.2	15.1	1000
0.7	0.6	10^7	8.57×10^5	0.1	1.57×10^7	162^3	16.6	15.6	1000
0.7	0.6	10^7	2.57×10^6	0.3	1.86×10^7	162^3	17.4	16.4	1000
0.7	0.6	10^7	4.29×10^6	0.5	2.14×10^7	162^3	18.1	17.0	1000
0.7	0.6	10^7	6.00×10^6	0.7	2.43×10^7	162^3	18.8	17.6	1000
0.7	0.6	10^7	8.57×10^6	1	2.86×10^7	162^3	19.7	18.5	1000
0.7	0.6	1.5×10^7	1.29×10^7	1	4.29×10^7	216^3	22.1	20.7	1000
0.7	0.6	1.8×10^7	1.03×10^7	0.67	4.29×10^7	216^3	22.0	20.6	1000
0.7	0.6	2.1×10^7	7.71×10^6	0.43	4.29×10^7	216^3	22.1	20.7	1000
0.7	0.6	2.4×10^7	5.14×10^6	0.25	4.29×10^7	216^3	21.9	20.5	1000
0.7	0.6	2.7×10^7	2.57×10^6	0.11	4.29×10^7	216^3	21.9	20.5	1000
0.7	0.6	3×10^7	0	0	4.29×10^7	216^3	22.0	20.6	1000
0.7	0.6	3×10^7	2.57×10^6	0.1	4.71×10^7	216^3	22.6	21.2	1000
0.7	0.6	3×10^7	7.71×10^6	0.3	5.57×10^7	216^3	23.6	22.1	1000
0.7	0.6	3×10^7	1.29×10^7	0.5	6.43×10^7	216^3	24.6	23.0	1000
0.7	0.6	3×10^7	1.80×10^7	0.7	7.29×10^7	216^3	25.5	23.9	1000
0.7	0.6	3×10^7	2.57×10^7	1	8.57×10^7	216^3	26.8	25.1	1000
0.7	0.6	10^8	0	0	1.43×10^8	256^3	30.84	28.9	500
0.7	0.6	10^8	8.57×10^6	0.1	1.57×10^8	256^3	31.7	29.6	500
0.7	0.6	10^8	2.57×10^7	0.3	1.86×10^8	256^3	33.5	31.3	500
0.7	0.6	10^8	4.29×10^7	0.5	2.14×10^8	256^3	34.9	32.6	500
0.7	0.6	10^8	6×10^7	0.7	2.43×10^8	256^3	36.1	33.8	500
0.7	0.6	10^8	8.57×10^7	1	2.86×10^8	256^3	37.8	35.4	500

TABLE 1. Simulation parameters and time-averaged Nusselt numbers for the temperature Nu_T and water vapour Nu_e. The averaging time t_{avg} is given in the last column.

It is worth mentioning that the boundary conditions associated with our experiment and DNS are quite different, which might also be responsible for the differences observed in figure 3. In our DNS, the flux of the water vapour is set to be zero; such a condition is more close to the ideal case or the situation in nature, where vapour transport takes place in an infinite or large lateral convection domain without

Gr	Λ	Δ_T (K)	T_{bulk} (°C)	$Nu_{T,bot}$	$Nu_{T,top}$	$Nu_{e,bot}$	$Nu_{e,top}$	η_{DNS}	t_{avg}
2.86×10^6	1	10.0	35.0	10.3	10.3	10.4	8.98	0.864	500
2.86×10^6	1	10.0	40.0	10.3	10.3	10.4	8.95	0.861	500
2.86×10^6	1	10.0	45.0	10.4	10.4	10.4	9.07	0.872	500
2.86×10^6	1	10.0	50.0	10.3	10.3	10.3	8.94	0.871	500

TABLE 2. Simulation parameters and time-averaged Nu_T and Nu_e at both plates when condensation on the sidewall is considered. The correction coefficient η_{DNS} is defined as $Nu_{e,top}/Nu_{e,bot}$.

condensation. However, for the present experimental set-up, a sidewall is present and kept at constant temperature, and so condensation is inevitable. Although a correction has been made in §4, the validation of the method needs to be justified. As a test, we run several additional DNS by setting saturation vapour pressure at the sidewall, $e = e_s(T)$. As a result, there exits an outward vapour flux at the sidewall. The correction coefficient is then defined as $\eta_{DNS} = \langle \partial_z T \rangle_{top}/\langle \partial_z T \rangle_{bot}$. The tests are conducted at $Gr = 2.9 \times 10^6$, $\Lambda = 1$ with four bulk temperatures (table 2). The temperature difference between the two interfaces is $\Delta_T = 10$ K. We compare the correction coefficients acquired from DNS with those used for the experimental data (4.2) with similar parameters in the inset of figure 3. It is seen that both coefficients are insensitive to the changes in bulk temperature, and η_{DNS} is on average larger than η for the experiment by about 8 %. For the temperature, the adiabatic boundary condition we applied at the sidewall region may result in a slightly lower SHF than for the constant-temperature boundary condition (Stevens, Lohse & Verzicco 2014). We nevertheless consider this as a minor effect since the SHF accounts for less than 10 % of the total flux (figure 2*b*).

The fact that the two Nusselt numbers are almost the same can also be seen from figure 4, where simultaneous snapshots of the temperature and vapour pressure iso-surfaces are seen to be almost identical. For a close inspection, we show the contour plots of both temperature (dashed curve) and vapour field (solid curve) in figure 5, with the vertical cross-section in figure 5(*a*) and horizontal cross-section figure 5(*b*). It is seen that both fields indeed show similar features, especially near the top and bottom boundaries. The isolines of the temperature field nest in those of the vapour field, which is due to the fact that the thermal diffusivity is slightly smaller than the mass diffusivity of water vapour.

In figure 6(*a*), we show the parameter ranges explored in both experimental and DNS studies in the $1/\Lambda$–Gr plane. It is seen that under the present parameterization, the experimental data for four different bulk temperatures correspond to four sets of measurement, each with a fixed value of buoyancy ratio but varying Grashof number Gr. In contrast, if the more conventional Rayleigh numbers Ra_T and Ra_e were to be used instead, the experimental data will correspond to measurements with the two control parameters both varying at the same time. This is shown in figures 6(*b*) (experiment) and 6(*c*) (DNS), where Nu_e are plotted against both Ra_e and Ra_T. The corresponding experimental parameter space is shown as open squares in the bottom plane. Different colours denote different bulk temperatures, corresponding to those in figure 2. It is seen that the moisture transfer rate Nu_e depends on Ra_e and Ra_T in a complicated way and a simple functional form such as a power law is not applicable. This further shows that the parameter set $\{Gr, \Lambda, Pr, Sc\}$ proposed here is a suitable choice for studying the two-component convection system in the present case.
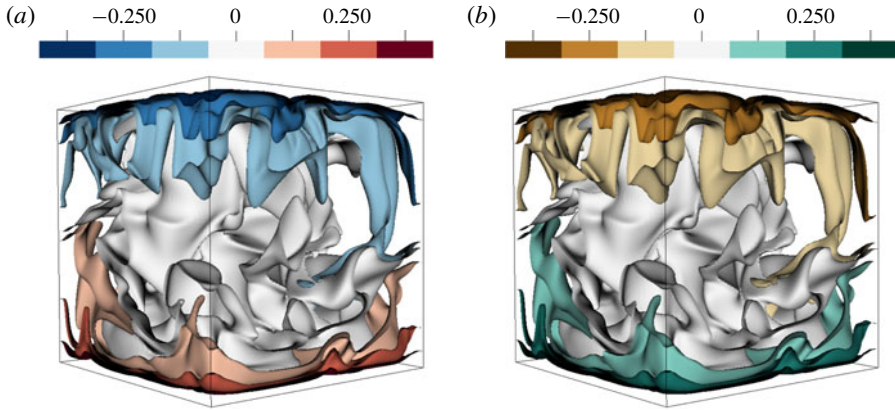
FIGURE 4. (Colour online) Snapshots of temperature (*a*) and water vapour content (*b*) isosurfaces taken simultaneously from DNS data at $Gr = 2.9 \times 10^7$, $\Lambda = 1$, $Pr = 0.7$ and $Sc = 0.6$.
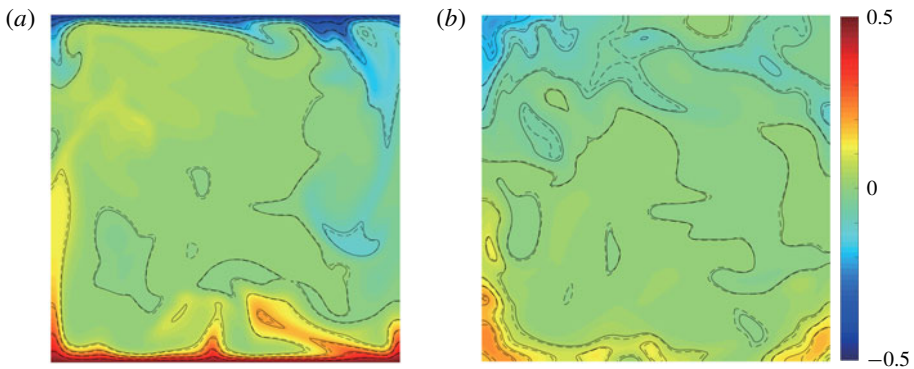

FIGURE 5. (Colour online) Contour plots of the temperature field (dashed curve) and vapour field (solid curve). (*a*) Snapshot of the vertical cross-section. (*b*) Snapshot of the horizontal cross-section. Colour map corresponding to the temperature fields.

6. The buoyancy ratio dependence

Although the two Nusselt numbers are mainly determined by the Grashof number, they may still have a weak dependence on the buoyancy ratio, which can be seen from figure 7. In this figure, the compensated Nu_e and Nu_T are plotted as functions of the inverse buoyancy ratio $1/\Lambda$ using the DNS data. To determine the possible functional form of $Nu(\Lambda)$, we use the two asymptotic limits of Λ as constraints. When $\Lambda = \infty$, the flow would be entirely temperature-driven and water vapour should act as a passive scalar (and vice versa when $\Lambda = 0$); these two limiting behaviours can be realized by the asymptotic function $(\Lambda Pr + Sc)/(\Lambda + 1)$. Fitting this to the data points in figure 7 and assuming a power-law dependence, we obtain

$$(Nu_e Gr^{-0.283})_{Pr=0.7, Sc=0.6} = 0.138 \left(\frac{Pr\Lambda + Sc}{\Lambda + 1} \right)^{-0.089}_{Pr=0.7, Sc=0.6}, \qquad (6.1)$$
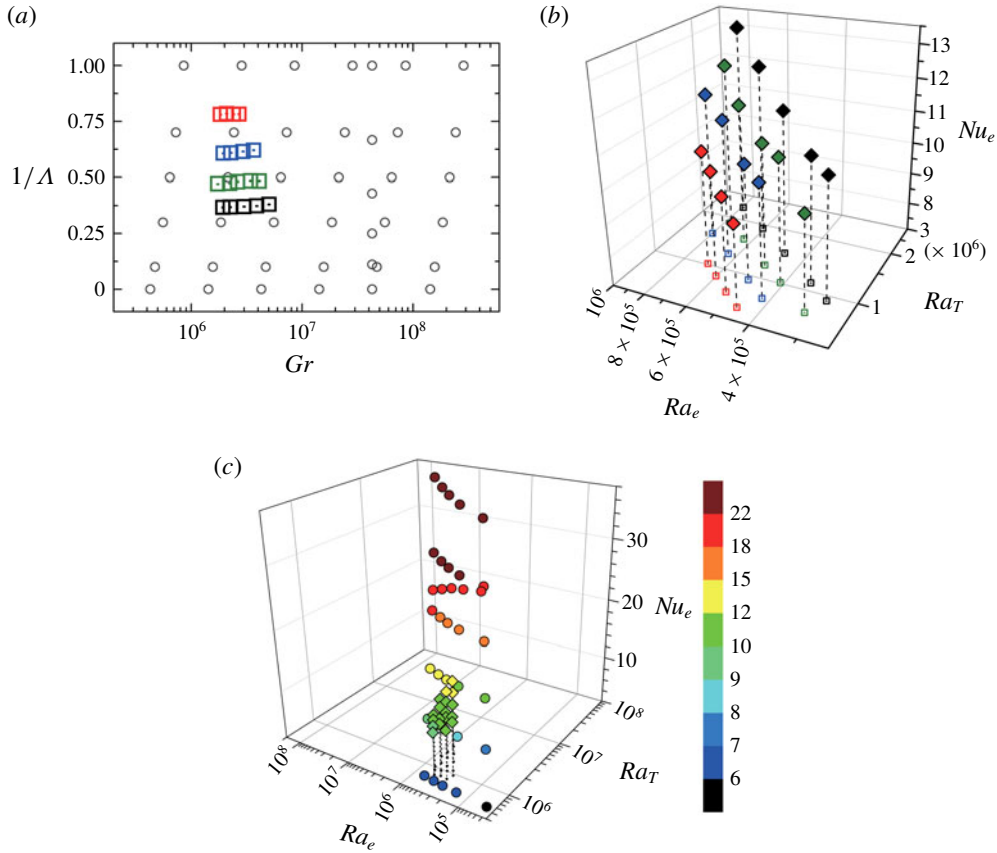
FIGURE 6. (Colour online) (*a*) Parameter space of the study in the $\{1/\Lambda, Gr\}$ plane; squares: experimental data; circles: DNS data. (*b*) Experimentally measured Nu_e as a function of Ra_T and Ra_e; open squares: projection of the data to the parameter space in the Ra_e, Ra_T plane. The colours in (*a,b*) correspond to different bulk temperatures and the colour code is the same as in figure 2(*a*). (*c*) Values of Nu_e from DNS.

$$(Nu_T Gr^{-0.283})_{Pr=0.7, Sc=0.6} = 0.147 \left(\frac{Pr\Lambda + Sc}{\Lambda + 1} \right)^{-0.087}_{Pr=0.7, Sc=0.6}. \tag{6.2}$$

Such a function incorporates the effect of buoyancy ratio Λ and would give the correct asymptotic limits.

7. The case when one of the scalars is passive

To demonstrate that the functional form used in (6.1) and (6.2) is justified, we consider the special case in which one of the scalars is active and the other is passive. Let temperature T be the active scalar and vapour pressure e be the passive one.

To deduce the Pr dependence of Nu_T, a minimum of two points are required. Here we choose $Nu_T(\Lambda = \infty, Pr = 0.6)$ and $Nu_T(\Lambda = \infty, Pr = 0.7)$. While for the Sc dependence of Nu_e, the values at $Nu_e(\Lambda = \infty, Pr = 0.7, Sc = 0.7)$ and $Nu_e(\Lambda = \infty, Pr = 0.7, Sc = 0.6)$ are selected. However, equations (6.1)–(6.2) are only valid for $Pr = 0.7$ and $Sc = 0.6$. We therefore consider two limiting cases as follows.
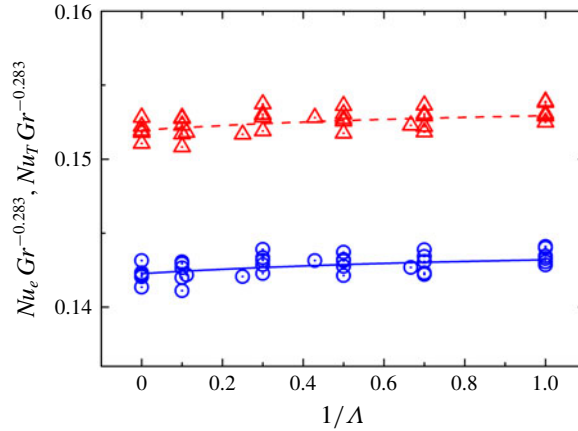
FIGURE 7. (Colour online) Compensated plot of Nu_e and Nu_T. Blue circles: $Nu_e Gr^{-0.283}$; red triangles: $Nu_T Gr^{-0.283}$; solid line: $0.138 Gr^{0.283}[(\Lambda Pr + Sc)/(\Lambda + 1)]^{-0.089}$; dashed line: $0.147 Gr^{0.283}[(\Lambda Pr + Sc)/(\Lambda + 1)]^{-0.087}$. The data scatter for the same Λ is about 2 % and is the uncertainty of the DNS data.

Taking advantage of the fact that the T and e fields are symmetric in the governing equations, we have $Nu_T(\Lambda = \infty, Pr = 0.6) = Nu_e(\Lambda = 0, Sc = 0.6)$ (where the quantity on the right-hand side can be acquired by substituting $\Lambda = 0$ into (6.1)). The second point can be obtained by substituting $\Lambda = \infty$ into (6.2), which gives $Nu_T(\Lambda = \infty, Pr = 0.7)$. Combining these two points, we obtain $Nu_T \sim Gr^{0.28} Pr^{0.34} = Ra_T^{0.28} Pr^{0.06}$, which is consistent with previously published results (Ahlers *et al.* 2009). Although the Pr dependence of Nu_T is determined by only two points, the fact that it agrees with known results suggests that the functional form of (6.1) and (6.2), which is deduced based on asymptotic limits and symmetry of the governing equations, is reasonable.

We now consider the Sc dependence of Nu_e. Note that when $Pr = Sc$ in (3.6) and (3.7), the two scalars are governed by the same equation, despite one being active and the other being passive. Therefore, Nu_e should be the same as Nu_T. Hence, $Nu_e(\Lambda = \infty, Pr = 0.7, Sc = 0.7) = Nu_T(\Lambda = \infty, Pr = 0.7, Sc = 0.7) = Nu_T(\Lambda = \infty, Pr = 0.7, Sc = 0.6)$, where the last equality comes about because when $\Lambda = \infty$, Nu_T does not depend on Sc, because the vapour is now a passive scalar. We now need another point to determine the Sc dependence of Nu_e, which can be obtained by substituting $\Lambda = \infty$ into (6.1), which yields $Nu_e(\Lambda = \infty, Pr = 0.7, Sc = 0.6)$. Combining these two points, we obtain the Schmidt number dependence of the passive scalar, i.e. $Nu_e \sim Gr^{0.28} Sc^{0.43}$. This implies that the transport of a passive scalar with large Schmidt number (or low molecular diffusivity), which is usually the case for liquid solvent, is much more efficient than that of an active scalar. To our knowledge, this is the first time that the Schmidt number dependence of passive scalar transfer rate has been predicted, which of course would need verification by future experiments.

8. A generalized Grossmann–Lohse theory

The Grossmann–Lohse (GL) theory (Grossmann & Lohse 2001, 2002; Stevens *et al.* 2013), which has demonstrated great success in predicting both the Nu and Re behaviours in turbulent RB convection, has been recently extended to two-scaler convection system (Yang *et al.* 2018). In this section, we extend the GL theory to

a two-component system using the new parameter set $\{Gr, \Lambda, Pr, Sc\}$. The basic idea of the GL theory is to divide the total energy and thermal dissipation rates into contributions from the boundary layer (BL) region and the bulk region:

$$\epsilon_u = \epsilon_{u,BL} + \epsilon_{u,bulk}, \tag{8.1}$$

$$\epsilon_\theta = \epsilon_{\theta,BL} + \epsilon_{\theta,bulk}, \tag{8.2}$$

$$\epsilon_e = \epsilon_{e,BL} + \epsilon_{e,bulk}. \tag{8.3}$$

Together with the exact relations for all three dissipation rates

$$
\begin{aligned}
\epsilon_u &= \frac{\nu^3}{H^4} Ra_T Pr^{-2}(Nu_T - 1) + \frac{\nu^3}{H^4} Ra_e Sc^{-2}(Nu_e - 1) \\
&= \frac{\nu^3}{H^4} Gr \frac{\Lambda}{\Lambda+1} Pr^{-1}(Nu_T - 1) + \frac{\nu^3}{H^4} Gr \frac{1}{\Lambda+1} Sc^{-1}(Nu_e - 1),
\end{aligned}
\tag{8.4}
$$

$$\epsilon_\theta = \kappa \frac{\Delta_T^2}{H^2} Nu_T, \tag{8.5}$$

$$\epsilon_e = D \frac{\Delta_e^2}{H^2} Nu_e, \tag{8.6}$$

we can obtain

$$Gr \frac{\Lambda}{\Lambda+1} Pr^{-1}(Nu_T - 1) + Gr \frac{1}{\Lambda+1} Sc^{-1}(Nu_e - 1) = c_1 \frac{Re^2}{g(\sqrt{Re_c/Re})} + c_2 Re^3, \tag{8.7}$$

$$
\begin{aligned}
Nu_T - 1 &= c_3 Re^{1/2} Pr^{1/2} \left\{ f\left[\frac{2aNu_T}{\sqrt{Re_c}} g\left(\sqrt{\frac{Re_c}{Re}} \right) \right] \right\}^{1/2} \\
&\quad + c_4 Pr Ref\left[\frac{2aNu_T}{\sqrt{Re_c}} g\left(\sqrt{\frac{Re_c}{Re}} \right) \right],
\end{aligned}
\tag{8.8}
$$

$$
\begin{aligned}
Nu_e - 1 &= c_3 Re^{1/2} Sc^{1/2} \left\{ f\left[\frac{2aNu_e}{\sqrt{Re_c}} g\left(\sqrt{\frac{Re_c}{Re}} \right) \right] \right\}^{1/2} \\
&\quad + c_4 Sc Ref\left[\frac{2aNu_e}{\sqrt{Re_c}} g\left(\sqrt{\frac{Re_c}{Re}} \right) \right],
\end{aligned}
\tag{8.9}
$$

where $c_1 = 8.05$, $c_2 = 1.38$, $c_3 = 0.487$, $c_4 = 0.0252$, $a = 0.922$ and $Re_c = (2a)^2$ are constants determined by existing data (Stevens *et al.* 2013). Here we have used the fact that the temperature and water vapour are equivalent to each other in this system and thus the prefactors in both (8.8) and (8.9) are the same (Yang *et al.* 2018). Now the three response parameters Re, Nu_T and Nu_e can be determined for given set of control parameters $\{Gr, \Lambda, Pr, Sc\}$.

We compare our experimental and numerical results with the predictions of the generalized GL theory in figure 8. The Prandtl number and Schmidt number are fixed to be $Pr = 0.7$ and $Sc = 0.6$, respectively. The dashed line (dark blue) corresponds to the prediction of the theory with density ratio equal to unity $\Lambda = 1$, while the solid line (deep red) represents infinite density ratio ($1/\Lambda = 0$). The generalized theory also predicts a negligible effect of density ratio on Nu_e. Furthermore, the Nu_e–Gr relation of the theory follows exactly the same trend as both our experimental and DNS results, despite some deviations at the lower end.
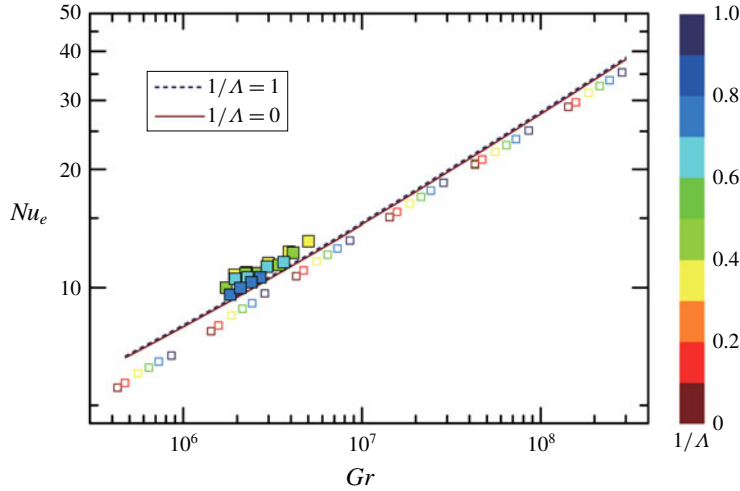
FIGURE 8. (Colour online) Nusselt number Nu_e as a function of Gr. Filled squares: experimentally measured Nu_e; open squares: Nu_e from DNS; solid line: $0.143Gr^{0.283}$; dashed line: GL prediction for $1/\Lambda = 1$; dotted line: GL prediction for $1/\Lambda = 0$; colour bar: inverse density ratio.

9. Implications for evaporation in nature

In hydrological cycles, the ocean is the ultimate source of all the water used in natural ecosystems and in human activity. Hence a comprehensive understanding of the worldwide ocean evaporation rate is necessary. However, the state-of-the-art bulk parameterization method (Liu 1979; Fairall *et al.* 1996) may not be accurate when the mean wind is low and thus mechanical driving is weak. In such circumstances, the SHF and LHF generated entirely by natural convection, as in the present case, may serve as a robust lower bound. This lower bound may be estimated by using relevant parameters corresponding to sea surface and in the atmosphere. We can express the Grashof number with bulk parameters: $Gr = 16[\alpha(SST - T_{bulk}) + \beta(e_s(SST) - e_{bulk})]gH^3/\nu^2$, where SST denotes the sea-surface temperature, T_{bulk} and e_{bulk} are the bulk temperature and bulk water vapour pressure, $e_s(SST)$ is the saturation vapour pressure at the sea surface and H is the reference height. The LHF is then $\Phi_L = Nu_e DL\Delta_{\rho,v}/H = 0.138Gr^{0.283}DL\Delta_{\rho,v}/H$, and the SHF is $\Phi_S = Nu_T k\Delta_T/H = 0.147Gr^{0.283}k\Delta_T/H$. Here we have neglected the buoyancy ratio effect, which has been shown to be insignificant for moist air. It should also be pointed out that the choice of reference height H has only a minor influence on the above estimation since the Grashof number has a cubical dependence on H.

10. Conclusion

We have presented in this study an indirect experimental method for measuring moisture transfer rates using natural convection as an example. We choose temperature and water vapour pressure as state variables for this two-component system. The non-dimensional moisture transfer rate Nu_e is determined indirectly from the total heat flux, after a correction for the sidewall condensation. We also made a DNS study of the system, to verify the experimental results and expand the parameter space. We find reasonable agreement between the experimental and numerical results. Moreover,

we propose to use the Grashof number Gr together with the buoyancy ratio Λ as control parameters, and find that the transfer rates for both heat (Nu_T) and water vapour (Nu_e) are mainly determined by the Grashof number Gr, and are only very weakly dependent on the buoyancy ratio Λ. We further find that $\{Gr, \Lambda, Pr, Sc\}$ form a full set of control parameters, and is more suitable than other choices for the present system. This set of parameters may also be applicable to describe other two-component systems. When one of the scalars is passive, its transport properties can also be inferred by considering the limiting cases. Moreover, the present results can be readily extended to the field of hydrology. An example is the no-wind evaporation limit of a water body, e.g. ocean, sea, lake or pond, which can be determined once the surface temperature, bulk temperature and bulk specific humidity are given. Therefore, the present results should complement existing bulk parameterization models for ocean evaporation.

REFERENCES

AHLERS, G., GROSSMANN, S. & LOHSE, D. 2009 Heat transfer and large scale dynamics in turbulent Rayleigh–Bénard convection. *Rev. Mod. Phys.* **81** (2), 503–537.

ANDREWS, D. G. 2000 *An Introduction to Atmospheric Physics*. Cambridge University Press.

ARYA, S. P. 1999 *Air Pollution Meteorology and Dispersion*. Oxford University Press.

BERGMAN, T. L., INCROPERA, F. P., DEWITT, D. P. & LAVINE, A. S. 2011 *Fundamentals of Heat and Mass Transfer*. Wiley.

BODENSCHATZ, E., MALINOWSKI, S. P., SHAW, R. A. & STRATMANN, F. 2010 Can we understand clouds without turbulence? *Science* **327** (5968), 970–971.

BRETHERTON, C. S. 1987 A theory for nonprecipitating moist convection between two parallel plates. Part I. Thermodynamics and linear solutions. *J. Atmos. Sci.* **44** (14), 1809–1827.

BRETHERTON, C. S. 1988 A theory for nonprecipitating convection between two parallel plates. Part II. Nonlinear theory and cloud field organization. *J. Atmos. Sci.* **45** (17), 2391–2415.

CANE, M. A., CLEMENT, A. C., KAPLAN, A., KUSHNIR, Y., POZDNYAKOV, D., SEAGER, R., ZEBIAK, S. E. & MURTUGUDDE, R. 1997 Twentieth-century sea surface temperature trends. *Science* **275** (5302), 957–960.

CHANDRAKAR, K. K., CANTRELL, W., CHANG, K., CIOCHETTO, D., NIEDERMEIER, D., OVCHINNIKOV, M., SHAW, R. A. & YANG, F. 2016 Aerosol indirect effect from turbulence-induced broadening of cloud-droplet size distributions. *Proc. Natl Acad. Sci. USA* **113** (50), 14243–14248.

CHILLÀ, F. & SCHUMACHER, J. 2012 New perspectives in turbulent Rayleigh–Bénard convection. *Eur. Phys. J.* E **35** (7), 58.

CHONG, K.-L., DING, G.-Y. & XIA, K.-Q. 2018 Multiple-resolution scheme in finite-volume code for active or passive scalar turbulence. *J. Comput. Phys.* **375**, 1045–1058.

DURACK, P. J., WIJFFELS, S. E. & MATEAR, R. J. 2012 Ocean salinities reveal strong global water cycle intensification during 1950 to 2000. *Science* **336**, 455–458.

EMANUEL, K. A. 1994 *Atmospheric Convection*. Oxford University Press.

FAIRALL, C. W., BRADLEY, E. F., HARE, J. E., GRACHEV, A. A. & EDSON, J. B. 2003 Bulk parameterization of air-sea fluxes updates and verification for the COARE algorithm. *J. Clim.* **16** (4), 571–591.

FAIRALL, C. W., BRADLEY, E. F., ROGERS, D. P., EDSON, J. B. & YOUNG, G. S. 1996 Bulk parameterization of air-sea fluxes for tropical ocean global atmosphere coupled ocean atmosphere response experiment. *J. Geophys. Res.* **101** (c2), 3747–3764.

GENT, P. R. & MCWILLIAMS, J. C. 1990 Isopycnal mixing in ocean circulation models. *J. Phys. Oceanogr.* **20** (1), 150–155.

GROSSMANN, S. & LOHSE, D. 2001 Thermal convection for large Prandtl numbers. *Phys. Rev. Lett.* **86**, 3316–3319.

GROSSMANN, S. & LOHSE, D. 2002 Prandtl and Rayleigh number dependence of the Reynolds number in turbulent thermal convection. *Phys. Rev.* E **66**, 016305.

HERNANDEZ-DUENAS, G., MAJDA, A. J., SMITH, L. M. & STECHMANN, S. N. 2013 Minimal models for precipitating turbulent convection. *J. Fluid Mech.* **717**, 576–611.

HUPPERT, H. E. & TURNER, J. S. 1981 Double-diffusive convection. *J. Fluid Mech.* **106**, 299–329.

LANDAU, L. D. & LIFSHITZ, E. M. 2013 *Fluid Mechanics*. Elsevier Science.

LEVITUS, S., ANTONOV, J. I., BOYER, T. P. & STEPHENS, C. 2000 Warming of the world ocean. *Science* **287**, 2225–2229.

LIU, W. T. 1979 Bulk parameterization of air-sea exchanges of heat and water vapor including the molecular constraints at the interface. *J. Atmos. Sci.* **36** (9), 1722–1735.

LOHSE, D. & XIA, K.-Q. 2010 Small-scale properties of turbulent Rayleigh–Bénard convection. *Annu. Rev. Fluid Mech.* **42** (1), 335–364.

MAIDMENT, D. R. 1993 *Handbook of Hydrology*. McGraw Hill Professional.

MANGARELLA, P. A., CHAMBERS, A. J., STREET, R. L. & HSU, E. Y. 1973 Laboratory studies of evaporation and energy transfer through a wavy air water interface. *J. Phys. Oceanogr.* **3** (1), 93–101.

MURRAY, F. W. 1967 On the computation of saturation vapor pressure. *J. Appl. Meteorol.* **6** (1), 203–204.

PAULUIS, O. & SCHUMACHER, J. 2011 Self-aggregation of clouds in conditionally unstable moist convection. *Proc. Natl Acad. Sci. USA* **108** (31), 12623–12628.

PRABHAKARAN, P., WEISS, S., KREKHOV, A., PUMIR, A. & BODENSCHATZ, E. 2017 Can hail and rain nucleate cloud droplets? *Phys. Rev. Lett.* **119** (12), 128701.

RADKO, T. 2013 *Double-Diffusive Convection*. Cambridge University Press.

SANDERS, C. J. & HOLMAN, J. P. 1972 Franz Grashof and the Grashof number. *Intl J. Heat Mass Transfer.* **15** (3), 562–563.

SCHMITT, R. W. 1994 Double diffusion in oceanography. *Annu. Rev. Fluid Mech.* **26** (1), 255–285.

SCHUMACHER, J. & PAULUIS, O. 2010 Buoyancy statistics in moist turbulent Rayleigh–Bénard convection. *J. Fluid Mech.* **648**, 509–519.

SHISHKINA, O., STEVENS, R. J. A. M., GROSSMANN, S. & LOHSE, D. 2010 Boundary layer structure in turbulent thermal convection and its consequences for the required numerical resolution. *New J. Phys.* **12** (7), 075022.

SINI, J. F., ANQUETIN, S. & MESTAYER, P. G. 1996 Pollutant dispersion and thermal effects in urban street canyons. *Atmos. Environ.* **30** (15), 2659–2677.

STEVENS, R. J. A. M., LOHSE, D. & VERZICCO, R. 2014 Sidewall effects in Rayleigh–Bénard convection. *J. Fluid Mech.* **741**, 1–27.

STEVENS, R. J. A. M., VAN DER POEL, E. P., GROSSMANN, S. & LOHSE, D. 2013 The unifying theory of scaling in thermal convection: the updated prefactors. *J. Fluid Mech.* **730**, 295–308.

VALLIS, G. K., PARKER, D. J. & TOBIAS, S. M. 2019 A simple system for moist convection: the Rainy–Bénard model. *J. Fluid Mech.* **862**, 162–199.

WEI, P., CHAN, T.-S., NI, R., ZHAO, X.-Z. & XIA, K.-Q. 2014 Heat transport properties of plates with smooth and rough surfaces in turbulent thermal convection. *J. Fluid Mech.* **740**, 28–46.

WEIDAUER, T., PAULUIS, O. & SCHUMACHER, J. 2010 Cloud patterns and mixing properties in shallow moist Rayleigh–Bénard convection. *New J. Phys.* **12**, 105002.

XIA, K.-Q. 2013 Current trends and future directions in turbulent thermal convection. *Theor. Appl. Mech. Lett.* **3** (5), 052001.

YANG, Y.-T., VERZICCO, R. & LOHSE, D. 2018 Two-scalar turbulent Rayleigh–Bénard convection: numerical simulations and unifying theory. *J. Fluid Mech.* **848**, 648–659.

ZHONG, J. Q., FUNFSCHILLING, D. & AHLERS, G. 2009 Enhanced heat transport by turbulent two-phase Rayleigh–Bénard convection. *Phys. Rev. Lett.* **102** (12), 124501.